Research Article | Vol. 31, No. 7 / 27 Mar 2023 / Optics Express 11249
Optics EXPRESS

Sub-diffraction computational imaging via a flexible multicore-multimode fiber

ZHOUPING LYU,[1,2,*] KSENIA ABRASHITOVA,[1] JOHANNES F. DE BOER,[2] ESBEN R. ANDRESEN,[3] HERVÉ RIGNEAULT,[4] AND LYUBOV V. AMITONOVA[1,2]

[1]*Advanced Research Center for Nanolithography (ARCNL), Science Park 106, 1098 XG Amsterdam, The Netherlands*
[2]*Department of Physics and Astronomy, Vrije Universiteit, De Boelelaan 1081, 1081 HV Amsterdam, The Netherlands*
[3]*Univ. Lille, CNRS, UMR 8523 - PhLAM - Physique des Lasers, Atomes et Molécules, F-59000 Lille, France*
[4]*Aix-Marseille Université, CNRS, Centrale Marseille, Institut Fresnel, Marseille, France*
[*]*z.lyu@arcnl.nl*

Abstract: An ultra-thin multimode fiber is an ideal platform for minimally invasive microscopy with the advantages of a high density of modes, high spatial resolution, and a compact size. In practical applications, the probe needs to be long and flexible, which unfortunately destroys the imaging capabilities of a multimode fiber. In this work, we propose and experimentally demonstrate sub-diffraction imaging through a flexible probe based on a unique multicore-multimode fiber. A multicore part consists of 120 Fermat's spiral distributed single-mode cores. Each of the cores offers stable light delivery to the multimode part, which provides optimal structured light illumination for sub-diffraction imaging. As a result, perturbation-resilient fast sub-diffraction fiber imaging by computational compressive sensing is demonstrated.

1. Introduction

Optical microscopy has long been the key tool in imaging small objects invisible to the naked eye especially in biological science. The main limitation of traditional light microscopy is the penetration depth [1]. High resolution optical imaging is only possible up to about 1 mm below the tissue surface because strong scattering blurs the image [2]. To bypass this problem, innovative microendoscopy techniques have been developed, including multicore fibers (MCFs) [3], fiber bundles [4], or gradient-index (GRIN) lens [5]. MCF endoscopy is hampered by the relatively large distance between the adjacent single-mode cores and therefore suffers from low resolution and pixelization effect [6,7]. Similarly, imaging quality of fiber bundle endoscopy is restricted by the core diameter, the proximity, and subsequent cross-talk. The main problems for GRIN lens endoscopes are the relatively large size and the limited field of view (FOV) [5,8]. Typically, the diameter of a GRIN lens varies from 0.5 mm to 1 mm [9].

Multimode fiber (MMF) endoscopy can overcome the pixelization problem and provide high resolution imaging [10,11]. However, MMF-based endoscopy is far from trivial. The output of a MMF is a random speckle pattern since the input information is scrambled by the interference and the coupling of fiber modes [12]. We can tailor the random speckle output of a MMF to a desired pattern at any plane using a spatial light modulator and a wavefront shaping approach [13–16]. For example, diffraction-limited foci behind the MMF can be generated to sequentially illuminate the sample for raster-scan endoscopy. The signal is then collected either in transmission or epi-direction with a single pixel detector [17–19]. The quality of raster-scan imaging relies on the quality of wavefront shaping. The ideal diffraction-limited focal spot can be generated with full control of fiber modes. In the situation of partial control, radially dependent focal spot aberration

#481052 https://doi.org/10.1364/OE.481052
Journal © 2023 Received 24 Nov 2022; revised 20 Feb 2023; accepted 28 Feb 2023; published 20 Mar 2023

Optics EXPRESS

arises [20,21]. Recently, a method of aberration-free high-resolution compressive MMF imaging has been demonstrated [22–24]. It uses structured illumination patterns, the sparsity of a sample, and compressive sensing algorithms to reconstruct images with sub-diffraction spatial resolution [25]. The imaging speed of 5 fps with spatial resolution more than 2-fold better than diffraction limit has been shown [24].

The main problem of all MMF-based imaging approaches is extreme sensitivity to fiber bending and vibration. The state-of-the-art methods ask for high stability of the MMF, in other words, the MMF should be kept motionless during the wavefront shaping, raster-scan imaging and compressive imaging. Small fiber perturbation changes the transmission matrix of the fiber, distorting the imaging result [26]. The straightforward approach is to use a rigid MMF [27]. However, many applications of endoscopy require a flexible probe. The proposed solutions include predicting the transmission matrix of deformed fiber by numerical simulation, which requires accurate characterization of fiber geometry [12]. Several methods to compensate the fiber bending with the extract feedback signal from distal fiber facet have been demonstrated [28–30]. Methods of imaging reconstruction under fiber bending with access only to the proximal facet are proposed [31–33]. However, the re-calibration step requires additional time and the imaging speed is limited by the algorithms and the transmission bandwidth of the hardware. Using mean speckle pattern recorded at different fiber positions in the calibration step makes the compressive imaging through MMF more robust to the fiber bending at the cost of fidelity [34]. It has been shown that a special graded-index MMF is more robust to the bending within a limited range [35]. Photonic lantern, fabricated by fiber tapering of a MCF followed by cutting at the middle of the collapsed part, can be used to solve the fiber deformation issue. However, the experimentally demonstrated spatial resolution was far from the diffraction limit [36].

In this work, we demonstrate sub-diffraction fiber imaging by using a specially designed multicore-multimode fiber (MCMMF). The multicore part consists of 120 Fermat's spiral distributed single-mode cores with a negligible cross-talk and is spliced to a multimode part. As long as each core is single-mode, the output intensity of each single-mode core is stable and will excite the same set modes of MMF. Thus, unlike the ordinary MMF, deformation of the multicore part of the MCMMF does not influence the output speckle pattern. The stability of the MCMMF based microendoscopy is experimentally demonstrated. The super-resolution imaging through the MCMMF probe is insensitive to 1 cm movement of the middle point of the 25 cm-long multicore part. The bending is achieved by moving the middle point at the free-hanging multicore part. The experimentally demonstrated spatial resolution is 1.5 times better than the diffraction limit. Our work demonstrates a flexible high-resolution imaging probe.

2. Methods

2.1. Experimental setup

All the experiments are performed using a custom-made MCMMF probe. As shown in Fig. 1(a), the MCMMF consists of the two spliced fibers: a 25 cm-long MCF and a 10 cm-long step-index MMF. The 120-core Fermat's spiral MCF is fabricated as described in [37] and its cross-section is depicted in Fig. 1(b). The MCF has a diameter of 220 µm and each individual fiber core diameter is 1.8 µm. Those cores are single-mode at 532 nm with negligible core-to-core cross-talk and distributed over a disc with a diameter of 75 µm. The average nearest-neighbor distance, Λ, is determined to be 6.4 µm. The MMF cross-section is presented in Fig. 1(c) and has an outer diameter of 220 µm, a core diameter of 200 µm, and a numerical aperture (NA) of 0.22. The multicore part is bending resilient since each single-mode core only guide one fundamental mode. This fundamental mode always simulates the same set of modes from MMF. Therefore the output speckle pattern of the MCMMF is stable under the single core injection if the multicore part is flexible and the multimode part is rigid. Although we use 10 cm-long multimode fiber in experiments, our simulations show that the length of the multimode part does not influence the

Optics EXPRESS

decorrelation properties of speckle patterns as far as it is longer than 5 mm. Therefore, the MMF can be short and small enough to act as a miniature stable minimally invasive probe.

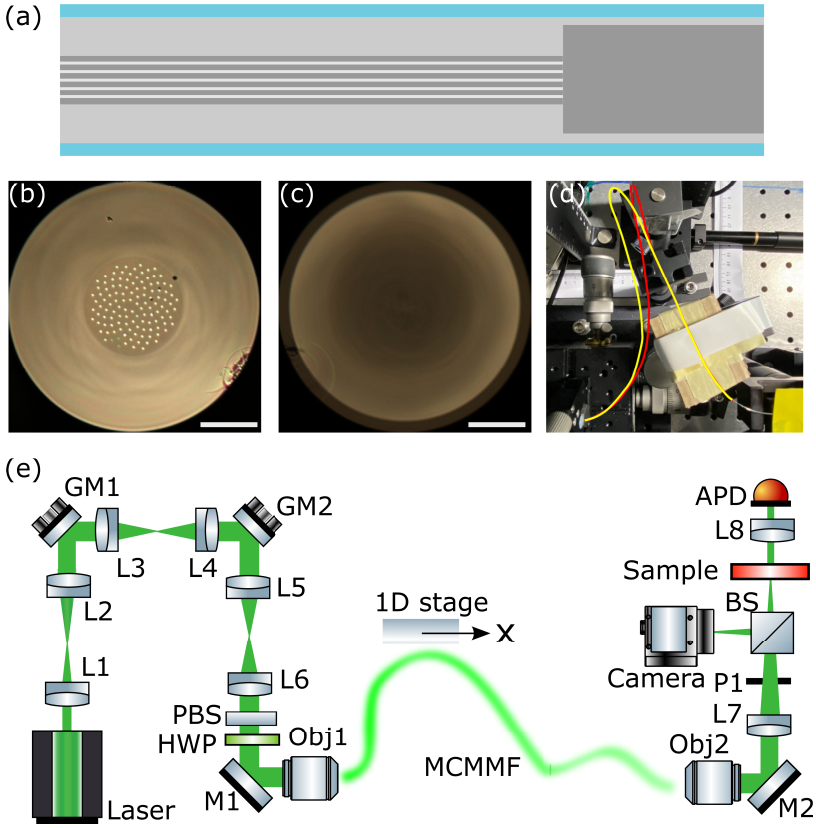

Fig. 1. (a) The schematic cross-section along the MCMMF probe that consists of a 25 cm-long MCF and a 10 cm-long MMF. (b),(c) Input (b) and output (c) facets of the MCMMF. At the input, 120 single-mode cores (a core diameter of 1.8 µm) are Fermat's spiral distributed. The scale bars are 50 µm. (d) Photo of the setup with stroke of the fiber at 0mm movement of 1D translation stage in red and 10mm movement of 1D translation stage in yellow. (e) Experimental setup for sub-diffraction imaging through a ultra-thin flexible fiber probe (L, lens; GM, galvo-mirror; PBS, polarization beam splitter; HWP, half wave plate; M, mirror; OBJ, objective; MCMMF, multicore-multimode fiber; P, pinhole; BS, beam splitter; APD, avalanche photodiode).

The experimental setup is illustrated in Fig. 1(e). We use a continuous wave (CW) linear polarized Nd:YAG laser [Cobolt Samba] with a wavelength of 532 nm. The beam is expanded by a 5.7× telescope (f1 = 35 mm, f2 = 200 mm) and then reflected by the pair of galvo-mirrors (Thorlabs GVS211/M). Two 1:1 4f systems project the galvo-mirrors to the entrance plane of the input objective (20x, NA = 0.4), by which the beam is coupled into the the MCMMF. The rotation of the pair of galvo-mirrors results in the movement of the focused beam at the proximal facet of the fiber. The polarization beam splitter and the half wave plate (HWP) control the input polarization. The multicore part of the MCMMF is free-hanging and attached to a 1D translation stage while the multimode part is fixed properly as shown in the Fig. 1(d). The output speckle pattern of the MCMMF is imaged onto the sample and the camera (Basler acA3088-57 µm, pixel size = 2.4 µm) with a M = 50 magnification by the output objective (40×, NA = 0.6, tube length 200 mm), lens7 (f7 = 250 mm) and a beam splitter. We cut the output speckle

Optics EXPRESS

pattern with an aperture so that the magnified FOV $(50 \times 57\ \mu m)^2$ is comparable to the sample area and multicore disc. Because the aperture is not on the image plane, high frequency can be cut. We estimate the NA = 0.21 by measuring the cut-off frequency of a speckle pattern in the Fourier domain. Therefore, the magnified imaging system has a diffraction limit of $D_{\text{lim}} = M \times \lambda/(2 \times NA) = 50 \times 0.532\ \mu m/(2 \times 0.21) = 63.5\ \mu m$. The intensity of light transmitted through the sample is focused by lens8 (f8 = 60 mm) on an avalanche photodiode (Thorlabs APD440A).

The proposed MCMMF imaging procedure consists of four main steps:

1. **Pre-calibration:** To locate the position of each core on the input. A 300×300 foci grid is sequentially projected to the input fiber facet and the total transmitted intensities are recorded. The transmission profile is first binarized by thresholding, so the cores are valued 1 while the background is 0. Then, the positions of $N_m = 120$ cores are extracted by calculating the center of mass of each binarized core.

2. **Speckles acquisition:** The beam is coupled to every single-mode core sequentially using the coordinates extracted during the pre-calibration step. The intensity distribution ($N \times N$ matrix) at the sample plane is recorded by the camera for each core. The $N_m \times N^2$ speckle illumination matrix ($\boldsymbol{A}$) is stored.

3. **Measurements:** The sample is inserted and imaging performed by coupling the light to each of the cores for sample illumination. The total signal transmitted through the sample is recorded with a single-pixel detector. As a result, the $N_m \times 1$ intensity vector ($\boldsymbol{y}$) is measured.

4. **Image reconstruction:** Illumination matrix $\boldsymbol{A}$ and intensity vector $\boldsymbol{y}$ are used to reconstruct the sample via ghost imaging and compressive sensing algorithms.

2.2. Image reconstruction algorithms

Post-processing is needed to reconstruct the image by solving an underdetermined problem:

$$\boldsymbol{A}\boldsymbol{x} = \boldsymbol{y}, \tag{1}$$

where the input $\boldsymbol{A}$ ($N_m \times N^2$) and $\boldsymbol{y}$ ($N_m \times 1$) are the known illumination matrix and measurement signal vector and $\boldsymbol{x}$ ($N^2 \times 1$) is the sample to be reconstructed. Here, one 2D speckle image ($N \times N$) is transformed to be 1D ($N^2 \times 1$) vector.

Ghost imaging (GI) reconstructs a sample by correlating an intensity vector given by an one-pixel detector and 2D illumination patterns [38]. It does not use any prior information and can provide the flatten image of a sample $\boldsymbol{x}_{\text{GI}}$ by [39]:

$$\boldsymbol{x}_{\text{GI}} = \frac{1}{N_m} \sum_{i=1}^{N_m} (\boldsymbol{y}_i - \langle \boldsymbol{y} \rangle) \boldsymbol{a}_i, \tag{2}$$

where $\boldsymbol{y}_i$ is the i^{th} intensity from the sample, $\langle . \rangle$ is ensemble averaging, and $\boldsymbol{a}_i$ is the i^{th} row of $\boldsymbol{A}$ meaning the i^{th} flatten speckle pattern. Usually, a large number of measurements is necessary to obtain diffraction-limited image via GI.

The alternative solution is to use a sparsity constraint and compressive imaging (CI) reconstruction [40–42]. Here we used two algorithms: total variation (TV) minimization `tval3` [41] and `tveq_logbarrier` [42], which both use the gradient sparse prior information with

Optics EXPRESS

equality constraints. Therefore, Eq. (1) can be solved:

$$\min_{\boldsymbol{x}} \sum_i \|D_i \boldsymbol{x}\|, \ s.t. \ \boldsymbol{A}\boldsymbol{x} = \boldsymbol{y}, \tag{3}$$

where $D_i\boldsymbol{x}$ is the discrete gradient of $\boldsymbol{x}$ at pixel i, $\|\cdot\|$ is l_2-norm. Those total variation minimization algorithms can give sharper edge and smooth field due to the gradient sparse assumption [43]. The difference between `tval3` and `tveq_logbarrier` is the way to solve the TV minimization: `tval3` use the Augmented Lagrangian method [41] and `tveq_logbarrier` use log barrier method [43]. We use the total variation (TV) minimization algorithm `tval3` with the result of `tveq_logbarrier` as an initial guess.

3. Results and discussion

3.1. Fiber characterization

In the first set of experiments, we characterize our MCMMF probe. First, we measure the positions of the individual cores. The square grid of 300×300 foci scans over 75 μm × 75 μm area at the fiber input facet with the step of 0.25 μm. For each focus spot, the total transmitted intensity of the fiber output is measured. The recorded transmission profile is shown in Fig. 2(a). We can see 120 bright dots that correspond to the individual cores. Three of the cores appear larger and brighter (labeled in Fig. 2(a) by red circles). This fiber is known to have three defects, as three cores are slightly bigger than the rest, and that these cores are multimode. To extract the position of each core, the transmission map is binarized. Every bright area is labeled as a core and the centroid of each core is calculated. An example of a speckle illumination pattern at the sample plane with the closed pinhole when light is coupled to one single-mode core is presented in Fig. 2(b). In Fig. 2(c) we show a simulated speckle of the MCMMF with a black circle indicating the FOV cropped by the pinhole. The pattern after the pinhole is shown in Fig. 2(d).

We define the sampling ratio as the ratio between the number of measurements N_m and the number of smallest resolvable features in the FOV: $R = N_\mathrm{m}\frac{S_\mathrm{feat}}{S_\mathrm{fov}}$. The target feature size $S_\mathrm{feat} = \pi\left(\frac{D_\mathrm{lim}}{(2\times1.5)}\right)^2 = 1407.5\ \mu\mathrm{m}^2$ was set to 1.5 times smaller than the diffraction limit. The experimental FOV is $S_\mathrm{fov} = D_\mathrm{fov}^2 = (57\ \mu\mathrm{m} \times M)^2 = 8.1\ \mathrm{mm}^2$. Therefore, the $R = 0.02$, which is very low.

Second, we measure the overall stability of the MCMMF probe. After pre-calibration, the coordinates of single-mode cores are saved. The speckle pattern acquisition step is repeated every 20 minutes for a total of 8 hours. In every step, the light is sequentially coupled to each core according to coordinates, and the intensity distribution of output speckle patterns is recorded. The correlation coefficient γ between the first measured speckle pattern and speckle patterns at different time is calculated for each core separately.

$$\gamma = \frac{\sum_i \sum_j (S_{ij} - \bar{S})(P_{ij} - \bar{P})}{\sqrt{(\sum_i \sum_j (S_{ij} - \bar{S})^2)(\sum_i \sum_j (P_{ij} - \bar{P})^2)}}, \tag{4}$$

where S and P are speckle patterns measured at zero time and with a certain delay, $\bar{S}$ and $\bar{P}$ are the mean values. The correlation of the speckle patterns of cores at different time with the first set of speckle patterns measured at $t = 0$ is shown in Fig. 2(e). The x-axis represents the time delay with respect to the first measurement and the y-axis represents the data for individual cores. Overall, the correlation is higher than 0.95 except those three defect cores. Those three defect cores are multimode cores. Therefore, the MCMMF output for those input cores is not stable. In all of the following measurements, those three defect cores are left out. Therefore, we have only 117 single-mode cores in the MCMMF and hence $N_\mathrm{m} = 117$ for the compressive imaging matrix.

Optics EXPRESS

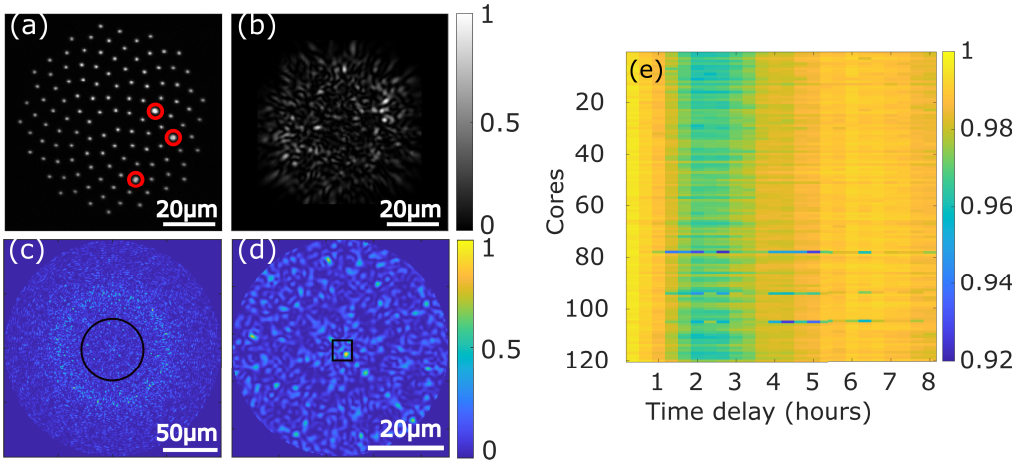

Fig. 2. (a) Transmission profile of the MCMMF for a dense grid of 300 × 300 sequentially projected focal spots at the input facet. (b) An experimental speckle pattern measured at the sample location with the closed pinhole when light is coupled to a single input core. (c) Simulated speckle on the MCMMF output. The black circle indicates experimental FOV. (d) The simulated speckle pattern after the pinhole. The black square indicates the FOV after numerical cropping. (e) Correlation coefficient, γ, between the first measured speckle pattern and speckle patterns at different times calculated for each core on the fiber input as a function of time.

Third, we analyze how is the decorrelation between speckles influenced by the length of the multimode part, the single-mode core structure of the multicore part, and the numerical cropping of the speckle patterns. For the best imaging performance, the sensing matrix generated by the MCMMF must be uncorrelated within itself. To analyze the decorrelation properties of the speckle patterns for different lengths of a multimode part, we performed numerical simulations. We analytically solve the wave equation in a cylindrical geometry with known boundary conditions and compute the electromagnetic field distributions and the propagation constants of all the modes of a multimode part. Light propagation through a multimode fiber is supported by a finite set of Linearly Polarized (LP) modes under the weak guidance approximation [44]. The simulations are performed for single-mode input cores arranged in the Fermat's spiral structure with different multimode fiber part lengths: 10 cm, 1 cm, and 0.5 cm. We calculated the decorrelation properties of the resulting speckle patterns by cross-correlation coefficient γ (Eq. (4)). As shown in Fig. 3(a), the correlation coefficient histograms for 10 cm (yellow), 1 cm (orange), and 0.5 cm (blue) long multimode almost coincide. Our simulations show that the length of a multimode part does not influence the decorrelation properties of generated speckle patterns as far as it is longer than 5 mm. We also simulate light propagation through the modified MCMMF probe where 121 single-mode cores are organized in a square grid of 70 by 70 μm with 7 μm step in-between. The cross-correlation coefficient histograms of output speckle patterns are shown in Fig. 3(b) and are very similar to the histograms of the original Fermat's spiral fiber. We conclude that the arrangement pattern of single-mode cores does not play a significant role. In Fig. 3(c) we plot cross-correlation coefficient histograms of experimentally measured speckle patterns within the full FOV (green) and after numerical cropping (pink). The distribution for experimentally measured patterns before the numerical crop is similar to the simulated one (yellow in Fig. 3(a)). After cropping, the width of the histogram is wider. However, we have maximum $N_m = 117$ independent measurements. The relatively low number of measurements can lead to constraints on the complexity of the sample.

Optics EXPRESS

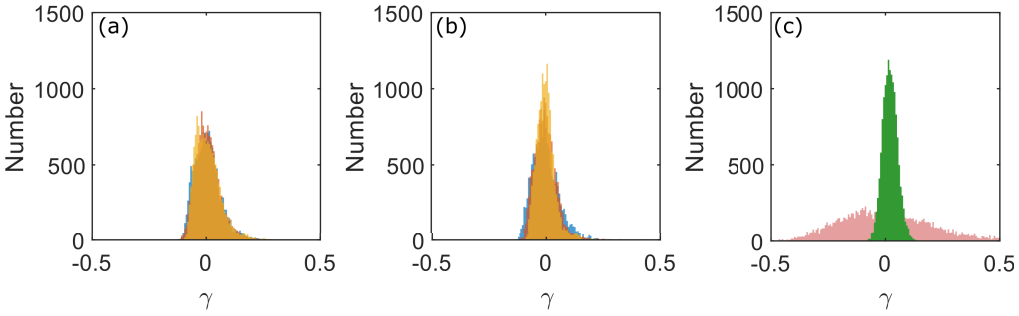

Fig. 3. Histograms of the cross-correlation coefficient between every two speckles of the MCMMFs with different parameters. (a),(b) Simulations of MCMMF with 117 Fermat's spiral distributed single-mode cores (a) and with 121 single-mode cores arranged in a square grid (b) for different lengths of a multimode part: 10 cm (yellow), 1 cm (orange), and 0.5 cm (blue). (c) Cross-correlation coefficient histograms for experimentally measured speckle patterns before (green) and after (pink) numerical FOV cropping.

3.2. *Sub-diffraction fiber imaging*

In the second set of experiments, we perform imaging through the MCMMF and investigate the resolution limit. We use two samples that are designed to have a characteristic feature size smaller than the diffraction limit of our imaging system. They are made by wet etching thick aluminium film on a glass slide. Maskless laser photolithography is used to define the pattern in the photo resist. At the wet etching step exposed pattern is transferred in the aluminium film. The samples are presented in Fig. 4(d),(g) and consist of two transparent holes in the aluminium film. The diameter of a hole and the distance between two holes are 50 µm (Fig. 4(d)) and 40 µm (Fig. 4(g)), which correspond to a feature size of $0.79D_{\text{lim}}$ and $0.68D_{\text{lim}}$, respectively.

After the pre-calibration and speckle acquisition steps, we install the sample and illuminate it by sequential core-by-core scan. The total intensity transmitted through the sample, $\boldsymbol{y}$, has been recorded. The reconstruction results for sample1 are shown in Fig. 4(b) for the GI and in Fig. 4(c) for the CI. In contrast to GI, CI can nicely reconstruct the sample without visible artifacts in the surrounding areas. However, due to the low sampling ratio ($R = 0.02$), we cannot resolve the two circles.

To enhance imaging resolution, we artificially increase R by cropping the FOV during the postprocessing to $S_{\text{fov}} = 54056$ µm^2 as presented in the black square in the Fig. 2(d). We now work in the oversampling regime, $R = 3$, as a high sampling rate is required for faithful image reconstruction. The results are presented in Fig. 4(d)-(i). For both samples, GI does not allow to reconstruct the images. In contrast, CI provides good image quality for sub-diffraction features. The higher intensity of the left hole can be explained by the slight tilt of the camera and/or the sample holder. Our MCMMF probe can achieve super-resolution, which is attributed to sample's sparsity, at a cost of limited FOV. As the optimal number of measurements should be comparable to the sparsity of the sample, imaging of more complex structures may require a higher number of measurements [45]. The number of measurements can in principle be increased by adding more single-mode cores. Our experimental results already demonstrate imaging through the MCMMF with a resolution 1.5 times better than the diffraction limit.

3.3. *Imaging through a flexible MCMMF probe*

In the final set of measurements, we demonstrate MCMMF-based imaging through a flexible probe. We experimentally investigate how does the deformation of the MCMMF influence the imaging quality. The middle point of multicore part of the fiber is fixed on a 1D translation stage,

Optics EXPRESS

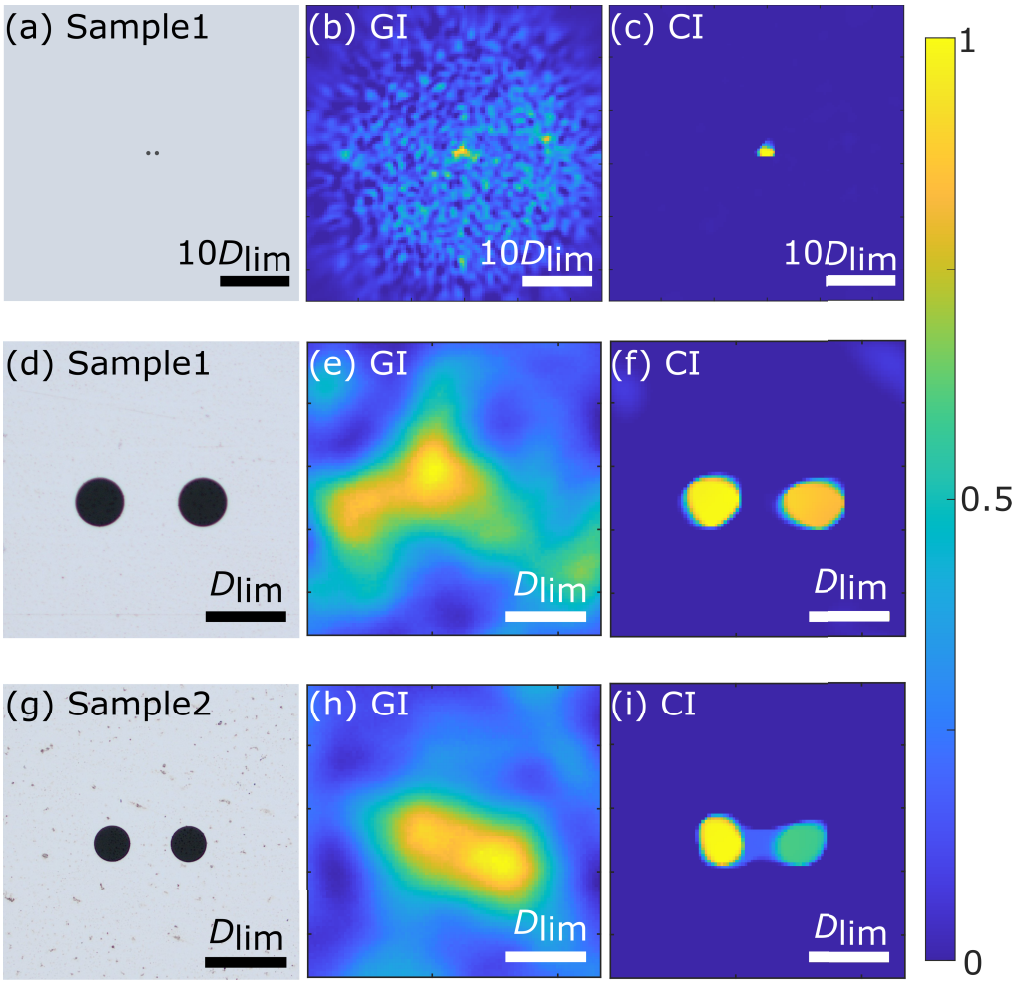

Fig. 4. Experimental results. (a)-(c) sample1 (a), Ghost imaging GI (b), and Compressive imaging CI (c) reconstruction results within the experimental FOV. (d), (g) High-resolution microscope images of sample1 (d) and sample2 (g). The diameter of a hole and the distance between two holes are 50 μm (sample1) and 40 μm (sample2), which correspond to a feature size of $0.79D_{\mathrm{lim}}$ and $0.68D_{\mathrm{lim}}$, respectively. (e), (h) GI and (f), (i) CI reconstruction results after FOV cropping during the postprocessing. The scale bars represent the diffraction limit of our imaging system D_{lim} = 63.5 μm (d)-(i) and $10D_{\mathrm{lim}}$ = 635 μm (a)-(c).

Optics EXPRESS

as shown in Fig. 1(d). The fiber deformation is controlled by the movement of the stage. The cores are not polarization maintaining so we could expect that output speckle patterns alter with the change of incident polarisation. Therefore, we first investigate the relation between the laser polarization and the intensity distribution on the output. We measure the speckle patterns at the sample plane for different linear polarization states coupled to a single-mode core on the fiber input by rotating the HWP. The correlation coefficient between the speckle pattern measured at a zero-angle HWP position and the speckle pattern at α-angle position of a HWP is calculated for each of the cores and α varied from 0 to 360°. The results are shown in Fig. 5(a). As expected, the speckle patterns change with a period of $\pi/2$ of the HWP angle. However, the intensity changes are really small such that the correlation coefficient drops only to about 0.97. Our results clearly indicate that the speckle patterns are robust against polarization instability. High correlation between the speckle patterns for two orthogonal input polarizations can be explained by mode structure that simplifies into a degenerated set of Linearly Polarized modes if the refractive index contrast is small (the weakly guided approximation).

Second, we investigate the stability of the output speckle patterns against fiber bending. The stage with the fiber moves from 0 mm to 10 mm with a 0.5 mm step. The fiber configurations at 0 mm and 10 mm are depicted in Fig. 1(d) by strokes in red and yellow color, respectively. For each position of the fiber probe, we couple light to each input core and measure the output speckle pattern. The experimental results presented in Fig. 5(b) show that the light intensity distribution at the fiber output is stable even if the fiber probe moves. The color represents the correlation coefficients between patterns measured at different MCMMF positions with the original speckle pattern measured before fiber moves (0 mm position). The result for each input core is measured separately and presented as a row in Fig. 5(b). Overall, the correlation coefficients are higher than 0.94, means that the illumination patterns are insensitive to the fiber displacements.

To investigate the sensitivity of MCMMF imaging to fiber bending, we repeat the measurements of sample1 while the stage with the fiber moves from 0 mm to 10 mm, as shown in Fig. 1(d). The pre-calibration and speckle acquisition steps have been done at 0 mm point. Then we move the fiber stage and record the signal. The signal acquisition time is 12 s for each position of the fiber. The speed is limited by the operation frequency and the setting time of galvo-mirror and can reach 0.12 s per measurement. The results are shown in Fig. 5(c), where the cross-correlation coefficients between the ground truth and the experimentally measured images are presented as a function of fiber displacement by yellow circles for CI and blue circles for GI. The acquired images are shown in insets for every 2 mm step. For both imaging approaches the experimentally measured images remain stable with fiber bending for all the fiber positions within 10 mm range, which is limited by the stage maximum travel range. Compressive imaging via MCMMF probe matches well with the original sample resolving two circles at a distance smaller than the diffraction limit of our system.

Optics EXPRESS

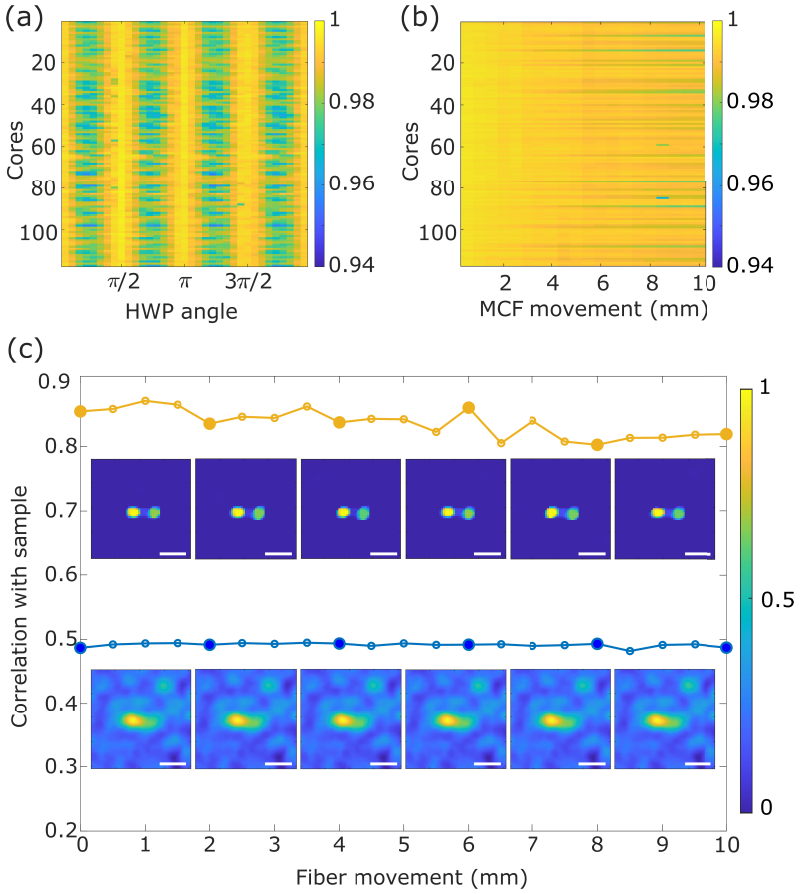

Fig. 5. (a) Correlation coefficients of speckles measured at different HWP angles with the speckle pattern measured when the HWP fast axis coincides with the input laser polarization (zero-angle position) as a function of HWP angle (horizontal axis) and a core number (vertical axis). (b) Correlation coefficients of speckle patterns measured at different MCMMF positions with the original speckle pattern measured before fiber moves. (c) Imaging quality as a function of fiber movement. The reconstruction quality is characterized by cross-correlation coefficient between the ground truth and ghost imaging (blue) and compressive imaging (yellow) results. Experimentally measured sample images at every 2 mm position are shown as insets. The scale bars are $2D_{\mathrm{lim}}$.

Optics EXPRESS

4. Conclusion

To summarize, we propose and experimentally demonstrate a ultra-thin and flexible MCMMF probe that overcomes the longstanding problem of multimode fiber imaging and allows for high-speed sub-diffraction imaging while the fiber is bending. Spatial resolution 1.5 times better than the diffraction limit has been experimentally demonstrated via the novel MCMMF probe. We demonstrate exceptional imaging stability over time and against polarization changes and fiber movements within a range of at least 10 mm. Our simulation shows the multimode fiber can be as short as 5 mm which proves the potential of being a miniature stable minimally invasive probe. Our work provides flexible high-resolution imaging probe and paves the way toward super-resolution in-vivo endomicroscopy.

Funding. Nederlandse Organisatie voor Wetenschappelijk Onderzoek; Agence Nationale de la Recherche.

Acknowledgments. This work has been partially carried out within ARCNL, a public-private partnership between UvA, VU, NWO and ASML, and was financed by 'Toeslag voor Topconsortia voor Kennis en Innovatie (TKI)' from the Dutch Ministry of Economic Affairs and Climate Policy. Parts of this work were developed at IRCICA (USR CNRS 3380, https://ircica.univ-lille.fr/) using FiberTech Lille facilities (https://fibertech.univ-lille.fr/en/). This work was supported by the French Ministry of Higher Education and Research, the 'Hauts de France' Regional Council, the European Regional Development fund (ERDF) through the CPER 'Photonics for Society'. We thank Sergey Amitonov for custom-made samples, Benjamin Lochocki for fruitful discussions and Marco Seynen for his help in programming the data acquisition software.

Disclosures. The authors declare no conflicts of interest.

Data availability. Data underlying the results presented in this paper are not publicly available at this time but may be obtained from the authors upon reasonable request.

References

1. V. Ntziachristos, "Going deeper than microscopy: the optical imaging frontier in biology," Nat. Methods **7**(8), 603–614 (2010).
2. F. Helmchen and W. Denk, "Deep tissue two-photon microscopy," Nat. Methods **2**(12), 932–940 (2005).
3. E. R. Andresen, S. Sivankutty, V. Tsvirkun, G. Bouwmans, and H. Rigneault, "Ultrathin endoscopes based on multicore fibers and adaptive optics: a status review and perspectives," J. Biomed. Opt. **21**(12), 121506 (2016).
4. B. A. Flusberg, A. Nimmerjahn, E. D. Cocker, E. A. Mukamel, R. P. Barretto, T. H. Ko, L. D. Burns, J. C. Jung, and M. J. Schnitzer, "High-speed, miniaturized fluorescence microscopy in freely moving mice," Nat. Methods **5**(11), 935–938 (2008).
5. J. K. Kim, W. M. Lee, P. Kim, M. Choi, K. Jung, S. Kim, and S. H. Yun, "Fabrication and operation of grin probes for in vivo fluorescence cellular imaging of internal organs in small animals," Nat. Protoc. **7**(8), 1456–1469 (2012).
6. D. Kim, J. Moon, M. Kim, T. D. Yang, J. Kim, E. Chung, and W. Choi, "Toward a miniature endomicroscope: pixelation-free and diffraction-limited imaging through a fiber bundle," Opt. Lett. **39**(7), 1921–1924 (2014).
7. G. Oh, E. Chung, and S. H. Yun, "Optical fibers for high-resolution in vivo microendoscopic fluorescence imaging," Opt. Fiber Technol. **19**(6), 760–771 (2013).
8. S. Ohayon, A. Caravaca-Aguirre, R. Piestun, and J. J. DiCarlo, "Minimally invasive multimode optical fiber microendoscope for deep brain fluorescence imaging," Biomed. Opt. Express **9**(4), 1492–1509 (2018).
9. M. A. Tadayon, I. Pavlova, K. M. Martyniuk, A. Mohanty, S. P. Roberts, F. Barbosa, C. A. Denny, and M. Lipson, "Microphotonic needle for minimally invasive endoscopic imaging with sub-cellular resolution," Sci. Rep. **8**(1), 10756 (2018).
10. E. E. Morales-Delgado, D. Psaltis, and C. Moser, "Two-photon imaging through a multimode fiber," Opt. Express **23**(25), 32158–32170 (2015).
11. L. V. Amitonova, A. Descloux, J. Petschulat, M. H. Frosz, G. Ahmed, F. Babic, X. Jiang, A. P. Mosk, P. S. J. Russell, and P. W. Pinkse, "High-resolution wavefront shaping with a photonic crystal fiber for multimode fiber imaging," Opt. Lett. **41**(3), 497–500 (2016).
12. M. Plöschner, T. Tyc, and T. Čižmár, "Seeing through chaos in multimode fibres," Nat. Photonics **9**(8), 529–535 (2015).
13. A. P. Mosk, A. Lagendijk, G. Lerosey, and M. Fink, "Controlling waves in space and time for imaging and focusing in complex media," Nat. Photonics **6**(5), 283–292 (2012).
14. T. Čižmár and K. Dholakia, "Shaping the light transmission through a multimode optical fibre: complex transformation analysis and applications in biophotonics," Opt. Express **19**(20), 18871–18884 (2011).
15. I. M. Vellekoop and A. Mosk, "Focusing coherent light through opaque strongly scattering media," Opt. Lett. **32**(16), 2309–2311 (2007).
16. I. N. Papadopoulos, S. Farahi, C. Moser, and D. Psaltis, "Focusing and scanning light through a multimode optical fiber using digital phase conjugation," Opt. Express **20**(10), 10583–10590 (2012).

Optics EXPRESS

17. S. Turtaev, I. T. Leite, T. Altwegg-Boussac, J. M. Pakan, N. L. Rochefort, and T. Čižmár, "High-fidelity multimode fibre-based endoscopy for deep brain in vivo imaging," Light: Sci. Appl. **7**(1), 92 (2018).
18. I. T. Leite, S. Turtaev, D. E. Boonzajer Flaes, and T. Čižmár, "Observing distant objects with a multimode fiber-based holographic endoscope," APL Photonics **6**(3), 036112 (2021).
19. T. Čižmár and K. Dholakia, "Exploiting multimode waveguides for pure fibre-based imaging," Nat. Commun. **3**(1), 1027 (2012).
20. A. Descloux, L. V. Amitonova, and P. W. Pinkse, "Aberrations of the point spread function of a multimode fiber due to partial mode excitation," Opt. Express **24**(16), 18501–18512 (2016).
21. Z. Lyu, G. Osnabrugge, P. W. Pinkse, and L. V. Amitonova, "Focus quality in raster-scan imaging via a multimode fiber," Appl. Opt. **61**(15), 4363–4369 (2022).
22. L. V. Amitonova and J. F. De Boer, "Compressive imaging through a multimode fiber," Opt. Lett. **43**(21), 5427–5430 (2018).
23. L. V. Amitonova and J. F. de Boer, "Endo-microscopy beyond the abbe and nyquist limits," Light: Sci. Appl. **9**(1), 81 (2020).
24. K. Abrashitova and L. V. Amitonova, "High-speed label-free multimode-fiber-based compressive imaging beyond the diffraction limit," Opt. Express **30**(7), 10456–10469 (2022).
25. E. J. Candes and M. B. Wakin, "An introduction to compressive sampling," IEEE Signal Process. Mag. **25**(2), 21–30 (2008).
26. M. Lan, D. Guan, L. Gao, J. Li, S. Yu, and G. Wu, "Robust compressive multimode fiber imaging against bending with enhanced depth of field," Opt. Express **27**(9), 12957–12962 (2019).
27. S. A. Vasquez-Lopez, R. Turcotte, V. Koren, M. Plöschner, Z. Padamsey, M. J. Booth, T. Čižmár, and N. J. Emptage, "Subcellular spatial resolution achieved for deep-brain imaging in vivo using a minimally invasive multimode fiber," Light: Sci. Appl. **7**(1), 110 (2018).
28. S. Farahi, D. Ziegler, I. N. Papadopoulos, D. Psaltis, and C. Moser, "Dynamic bending compensation while focusing through a multimode fiber," Opt. Express **21**(19), 22504–22514 (2013).
29. A. M. Caravaca-Aguirre, E. Niv, D. B. Conkey, and R. Piestun, "Real-time resilient focusing through a bending multimode fiber," Opt. Express **21**(10), 12881–12887 (2013).
30. R. Y. Gu, R. N. Mahalati, and J. M. Kahn, "Design of flexible multi-mode fiber endoscope," Opt. Express **23**(21), 26905–26918 (2015).
31. G. S. Gordon, M. Gataric, A. G. C. Ramos, R. Mouthaan, C. Williams, J. Yoon, T. D. Wilkinson, and S. E. Bohndiek, "Characterizing optical fiber transmission matrices using metasurface reflector stacks for lensless imaging without distal access," Phys. Rev. X **9**(4), 041050 (2019).
32. S. Li, S. A. Horsley, T. Tyc, T. Čižmár, and D. B. Phillips, "Memory effect assisted imaging through multimode optical fibres," Nat. Commun. **12**(1), 3751 (2021).
33. Z. Wen, Z. Dong, C. Pang, C. F. Kaminski, Q. Deng, J. Xu, L. Wang, S. Liu, J. Tang, W. Chen, X. Liu, and Q. Yang, "Single multimode fiber for in vivo light-field encoded nano-imaging," arXiv, arXiv:2207.03096 (2022).
34. M. Lan, Y. Xiang, J. Li, L. Gao, Y. Liu, Z. Wang, S. Yu, G. Wu, and J. Ma, "Averaging speckle patterns to improve the robustness of compressive multimode fiber imaging against fiber bend," Opt. Express **28**(9), 13662–13669 (2020).
35. D. E. B. Flaes, J. Stopka, S. Turtaev, J. F. De Boer, T. Tyc, and T. Čižmár, "Robustness of light-transport processes to bending deformations in graded-index multimode waveguides," Phys. Rev. Lett. **120**(23), 233901 (2018).
36. D. Choudhury, D. K. McNicholl, A. Repetti, I. Gris-Sánchez, S. Li, D. B. Phillips, G. Whyte, T. A. Birks, Y. Wiaux, and R. R. Thomson, "Computational optical imaging with a photonic lantern," Nat. Commun. **11**(1), 5217 (2020).
37. S. Sivankutty, V. Tsvirkun, O. Vanvincq, G. Bouwmans, E. R. Andresen, and H. Rigneault, "Nonlinear imaging through a fermat's golden spiral multicore fiber," Opt. Lett. **43**(15), 3638–3641 (2018).
38. Y. Bromberg, O. Katz, and Y. Silberberg, "Ghost imaging with a single detector," Phys. Rev. A **79**(5), 053840 (2009).
39. O. Katz, Y. Bromberg, and Y. Silberberg, "Compressive ghost imaging," Appl. Phys. Lett. **95**(13), 131110 (2009).
40. S. Foucart and H. Rauhut, "An invitation to compressive sensing," in *A Mathematical Introduction to Compressive Sensing* (Springer, 2013), pp. 1–39.
41. C. Li, W. Yin, H. Jiang, and Y. Zhang, "An efficient augmented lagrangian method with applications to total variation minimization," Comput. Optim. Appl. **56**(3), 507–530 (2013).
42. E. J. Candès, J. Romberg, and T. Tao, "Robust uncertainty principles: Exact signal reconstruction from highly incomplete frequency information," IEEE Trans. Inf. Theory **52**(2), 489–509 (2006).
43. C. Li, *An efficient algorithm for total variation regularization with applications to the single pixel camera and compressive sensing* (Rice University, 2010).
44. A. W. Snyder and J. D. Love, *Optical Waveguide Theory*, vol. 175 (Chapman and Hall London, 1983).
45. B. Lochocki, M. V. Verweg, J. J. Hoozemans, J. F. de Boer, and L. V. Amitonova, "Epi-fluorescence imaging of the human brain through a multimode fiber," APL Photonics **7**(7), 071301 (2022).